Available online at www.sciencedirect.com
SCIENCE DIRECT
Journal of Catalysis 234 (2005) 48–63
JOURNAL OF CATALYSIS
www.elsevier.com/locate/jcat

Hierarchical, multiscale surface reaction mechanism development: CO and H_2 oxidation, water–gas shift, and preferential oxidation of CO on Rh

A.B. Mhadeshwar, D.G. Vlachos *

Department of Chemical Engineering and Center for Catalytic Science and Technology, University of Delaware, Newark, DE 19716-3110, USA

Received 16 March 2005; revised 16 May 2005; accepted 26 May 2005

Available online 12 July 2005

Abstract

A hierarchical multiscale parameter refinement approach was used to develop microkinetic models for CO and H_2 oxidation, and CO–H_2 coupling for water–gas shift (WGS) and preferential oxidation (PROX) of CO on Rh. The rate parameters were estimated with a combination of quantum mechanical density functional theory (DFT), the semi empirical unity bond index-quadratic exponential potential method, and transition-state theory. To improve the predictive ability, selected pre-factors of the CO and H_2 oxidation reaction mechanisms were optimized against multiple experimental data sets, such as ignition, molecular beam, and laser-induced fluorescence. Thermodynamic consistency of rate parameters was ensured over a wide temperature range by a combination of statistical mechanics and constraints-based optimization. DFT calculations were used to estimate cross adsorbate–adsorbate CO–H interactions. It is shown that the coupling between the two fuels arising from these interactions is essential for PROX of CO. Important reaction pathways in the WGS and PROX chemistries are discussed. For example, it is shown that the oxidation of CO by OH via the carboxyl intermediate, and not by O, is the dominant path in PROX. Thus, hydrogen acts as a "catalyst" for CO combustion under certain conditions. Finally, the mechanisms are validated against additional sets of redundant experimental data.

Keywords: Microkinetic modeling; Hierarchical parameter refinement; Fuel processing; Carbon monoxide; Hydrogen; Catalytic combustion; Water–gas shift; Preferential oxidation; Thermodynamic consistency; Rhodium

1. Introduction

Fuel-cell technology is of recent interest for generating electricity because of its potential widespread applications, ranging from small-scale portable devices to stationary power generation and automobiles. Compared with conventional lithium batteries, fuel cells offer far higher energy densities, and they are less polluting and could be more efficient than internal combustion engines. H_2 acts as the fuel in proton exchange membrane (PEM) fuel cells. However, H_2 storage and transportation are a major problem in the widespread commercialization of PEM fuel cells. Furthermore, even minute amounts of CO in the H_2 fuel can poison the fuel-cell catalyst. Catalytic partial oxidation (CPOX) of natural gas on various transition metals can be used to produce syngas. Syngas produced by various means typically undergoes water–gas shift (WGS) reaction to convert CO to H_2

$$\mathrm{CO} + \mathrm{H_2O} \leftrightarrow \mathrm{CO_2} + \mathrm{H_2}. \quad (1)$$

To minimize the remaining CO content in the H_2 stream in order to avoid poisoning of the fuel-cell catalyst, preferential oxidation (PROX) of CO is typically carried out

$$\mathrm{CO} + \tfrac{1}{2}\mathrm{O_2} \rightarrow \mathrm{CO_2} \quad \text{and} \quad \mathrm{H_2} + \tfrac{1}{2}\mathrm{O_2} \rightarrow \mathrm{H_2O}. \quad (2)$$

All of these processes encompass the same fundamental chemistries of CO and H_2 adsorption, desorption, and combustion, as well as synergetic effects arising from using multiple fuels. This synergism was referred to in Ref. [1] as

* Corresponding author. Fax: +1-302-831-1048.
E-mail address: vlachos@che.udel.edu (D.G. Vlachos).

0021-9517/$ – see front matter
doi:10.1016/j.jcat.2005.05.016

$CO–H_2$ *coupling* (see Section 3 for a more detailed discussion).

Microkinetic modeling [2] offers an efficient approach to understanding the underlying chemistry and eventually design fuel processors used upstream of a PEM fuel cell. Obviously, the uniqueness of kinetic parameters that can explain certain experimental features still remains a problem under certain conditions. For example, we have found examples where even small changes in parameters can change the rate-determining step [1]. A number of microkinetic models have previously been proposed for natural gas CPOX and its subsets on Pt and Rh [3–10]. However, all of these mechanisms have some inherent limitations, as outlined in [11–14]. A primary reason for the lack of a single comprehensive predictive reaction mechanism is that most of these mechanisms are optimized against a single type of experimental data. A limited number of fundamental density functional theory (DFT)-based microkinetic models [15,16], for PROX and WGS on various transition metals, established the foundations for first-principles modeling but do not account for $CO–H_2$ coupling steps, adsorbate–adsorbate interactions, and catalyst heterogeneity. Most fitted mechanisms lack thermodynamic consistency, an essential feature for ensuring correct rate calculations, equilibrium composition, energy balance, and temperature profiles [17]. This becomes an essential issue when equilibrium limited reactions, such as WGS, are modeled at high temperatures.

Over the past few years, we have been developing techniques that overcome the above limitations [13,14,17] to describe CO oxidation [18,19], H_2 oxidation [1,13,14], and $CO–H_2$ coupling for WGS and PROX [1,20] on Pt. More recently, we have introduced a hierarchical multiscale approach [21] that combines quantum mechanical DFT with semiempirical methods to improve predictive capabilities with minimal computational cost. In brief, the approach is *hierarchical* in nature, since we start with simple theoretical tools (e.g., semiempirical estimation methods, mean field approximation, simple reactor models) to identify the important parameters, followed by refinement (iterative, if necessary) of these parameters only, with the use of advanced theoretical and computational tools (e.g., first-principles quantum mechanics, kinetic Monte Carlo, molecular dynamics, computational fluid dynamics). Our approach is *multiscale*, since tools and phenomena span a broad range of length and time scales, from the quantum to the reactor. Reviews of multiscale simulation can be found in [22,23]. Note that in conventional bottom-up multiscale simulation, nearly all tools are coupled. However, for complex systems, such as catalytic reactions on polycrystalline and supported catalysts, we advocate that only some of these higher-level theoretical tools should be used whenever judged necessary. Consequently, the hierarchical approach makes simulations feasible in reasonable computational times.

In this paper, we develop microkinetic models for CO and H_2 oxidation and for the WGS and PROX on Rh, using the hierarchical approach. The paper is organized as follows. The development of CO and H_2 catalytic oxidation mechanisms is discussed in Section 2 with pre-factor refinement against *targeted* experiments, which we identify via sensitivity analysis (SA) in Appendix A, and by ensuring thermodynamic consistency. These reaction mechanisms serve as building blocks for the more complex WGS and PROX reactions and to illustrate some elements of the reaction mechanism development. Section 3 is devoted to the development of a $CO–H_2$ coupling mechanism, along with an analysis of the important reaction pathways in WGS and PROX. Finally, further validation of the reaction mechanisms is presented in Appendix B.

2. CO and H_2 oxidation mechanisms on Rh

2.1. Experimental data on CO oxidation and H_2 oxidation on Rh

Sant and Wolf [24] carried out atmospheric pressure ignition experiments on a Rh/SiO_2 wafer with a mixture of CO, O_2, and N_2. The ignition temperature of CO/O_2 mixtures was found to increase with the inlet CO composition (Fig. 1). Molecular beam experiments were carried out by Gopinath and Zaera [25] on a Rh(111) single crystal to investigate the effects of temperature and inlet composition on the rate of CO_2 production (Figs. 2 and B.1). The CO_2 production rate versus temperature shows a maximum for all compositions. Coulston and Haller [26] studied the effect of temperature on the rate of CO_2 production on a Rh foil with molecular beam experiments. The CO_2 production rate exhibited a maximum (Fig. B.2). CO TPD (Fig. B.3), O_2 TPD, and $CO–O_2$ TPR (Fig. B.4) experiments on Rh(111) and Rh(100)

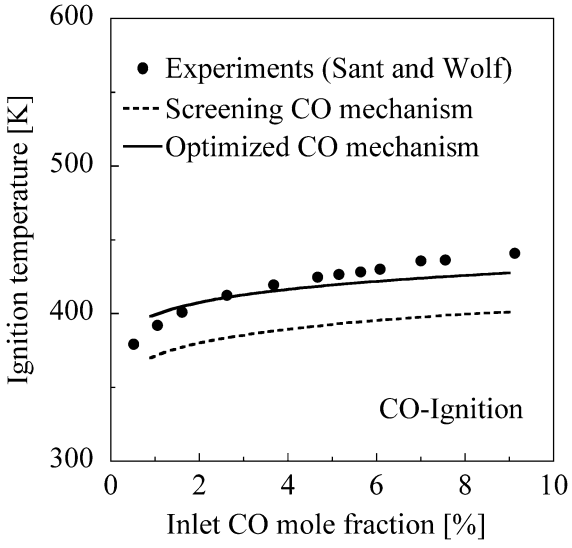

Fig. 1. Performance of the screening and optimized CO mechanisms against the CO-ignition experimental data of [24] at atmospheric pressure. Other operating conditions include a catalyst area of 5.67 cm^2, a reactor volume of 6 cm^3, and a residence time of ∼1.9 s.

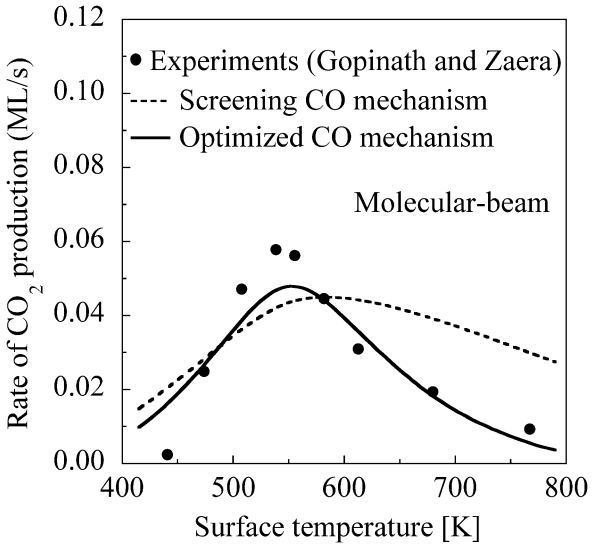

Fig. 2. Performance of the screening and optimized CO mechanisms against the molecular beam experimental data of [25]. The total inlet flux is 1 ML/s and the inlet composition is $CO/O_2 = 3/1$.

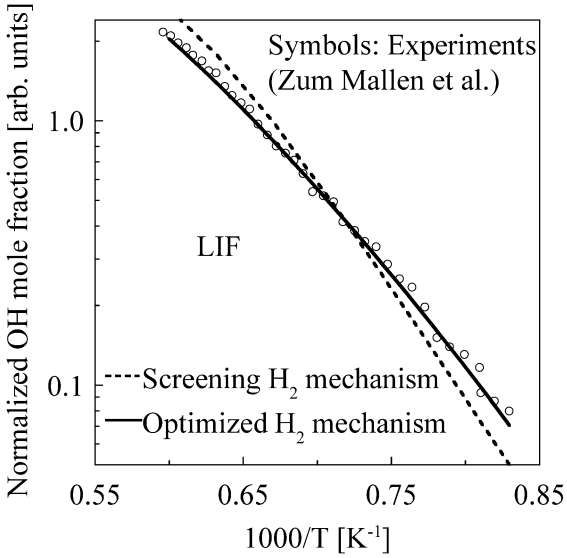

Fig. 4. Performance of the screening and optimized H_2 mechanisms against the laser induced fluorescence (LIF) experiments of [5]. The operating conditions include a pressure of 0.102 Torr (0.1 Torr O_2 and 0.002 Torr H_2), a reactor volume of 400 cm^3, and a catalyst area of 0.51 cm^2.

single crystals were investigated by several groups [27–29]. The desorption rates of CO and O were found to be coverage dependent.

To the best of our knowledge, ignition experiments for H_2 oxidation on Rh are not available in the literature; therefore, we have conducted such experiments in our laboratory at 1 atm with a Rh foil inserted into a metallic microreactor. The ignition temperature of H_2/O_2 mixtures was found to decrease with increase in the inlet H_2 composition (Fig. 3). Zum Mallen et al. [5] carried out laser-induced fluorescence (LIF) studies on a polycrystalline Rh foil with H_2/O_2 mixtures. The OH LIF signal was found to increase with increasing temperature (Fig. 4). H_2 TPD (Fig. B.5), H_2O TPD, and H_2–O_2 TPR (Fig. B.6) experiments on Rh(111), Rh(110), and Rh(100) single crystals were carried out by several groups [30–33]. The activation energy for H_2 desorption was found to be coverage dependent.

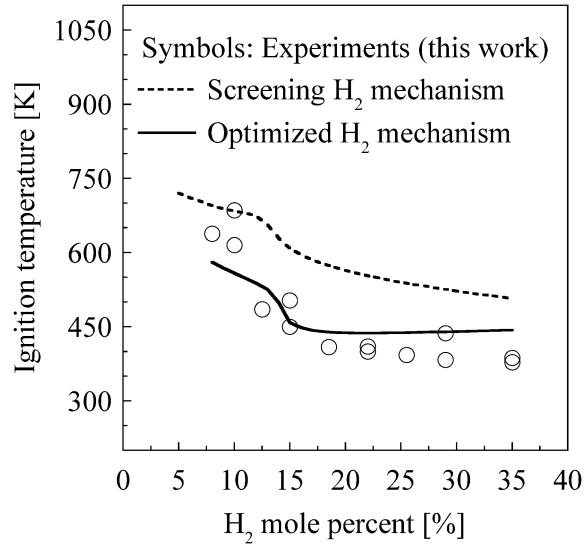

Fig. 3. Performance of the screening and optimized H_2 mechanisms against the H_2-ignition experimental data collected in our laboratory at atmospheric pressure in a microreactor. Other operating conditions include a reactor volume of 0.64 cm^3, a catalyst area of 1.56 cm^2, and a flow rate of 2 l/min (corresponding to a residence time of ∼20 ms).

2.2. *Screening surface reaction mechanisms, parameter estimation, and model assessment*

For the CO oxidation mechanism on Rh, we propose five reversible elementary-like steps (R_1–R_{10}), as shown in Table 1. Similarly, nine reversible elementary-like steps are proposed for H_2 oxidation (R_1–R_4 and R_{11}–R_{24}). The dissociative and atomic adsorption–desorption steps of oxygen (R_1–R_4) are common in both mechanisms. These and all other steps in our mechanism follow Langmuir–Hinshelwood kinetics. However, additional reactions, such as Eley–Rideal and steps involving subsurface species, could easily be included if information existed. We first make initial estimates of kinetics parameters to develop *screening* reaction mechanisms, and we use the mean-field approximation for all calculations. This process is outlined next.

Transition-state theory (TST)-based order-of-magnitude initial estimates of the pre-factors are taken to be 10^{13} s^{-1} for desorption steps and 10^{11} s^{-1} for Langmuir–Hinshelwood (LH)-type surface reactions [2]. The initial CO desorption pre-factor is taken to be 10^{16} s^{-1}, considering its typical range of 10^{14}–10^{18} s^{-1} [34]. Initial sticking coefficients of O_2, CO, H_2, and H_2O are taken to be 0.1, 0.9, 0.25, and 0.7, respectively, whereas those of the other species (O, CO_2, OH, and H) are assumed to be equal to 1. These initial sticking coefficients are similar to the ones in the screen-

Table 1
Surface reaction mechanisms for CO oxidation (R_1–R_{10}), H_2 oxidation (R_1–R_4 and R_{11}–R_{24}), and CO–H_2 coupling (R_1–R_{46}) for WGS and PROX reactions on Rh

No.	Reaction	Sticking coefficient (unitless) or pre-factor (s^{-1})	Temperature exponent β	Activation energy at 300 K (kcal/mol)
		Oxygen adsorption–desorption steps		
R_1	$O_2 + 2* \rightarrow 2O^*$	4.81×10^{-2}	1.997	0.0
R_2	$2O^* \rightarrow O_2 + 2*$	4.31×10^{12}	1.199	$80.9 - 42\theta_O + f(T)$
R_3	$O + * \rightarrow O^*$	4.45×10^{-2}	−1.895	0.0
R_4	$O^* \rightarrow O + *$	9.76×10^{12}	−1.999	$100 - 21\theta_O + f(T)$
		CO oxidation on Rh		
R_5	$CO + * \rightarrow CO^*$	5.00×10^{-1}	−2.000	0.0
R_6	$CO^* \rightarrow CO + *$	2.26×10^{14}	1.988	$38.5 - 17\theta_{CO} - 3.7\theta_H + f(T)$
R_7	$CO_2 + * \rightarrow CO_2*$	9.77×10^{-2}	−1.946	0.0
R_8	$CO_2* \rightarrow CO_2 + *$	1.13×10^{13}	1.800	$5.2 + f(T)$
R_9	$CO_2* + * \rightarrow CO^* + O^*$	2.04×10^{10}	1.545	$17.3 + f(\theta_O, \theta_H, \theta_{CO}, T)$ [a]
R_{10}	$CO^* + O^* \rightarrow CO_2* + *$	1.17×10^{9}	1.781	$23.5 + f(\theta_O, \theta_H, \theta_{CO}, T)$ [b]
		H_2 oxidation on Rh		
R_{11}	$H_2 + 2* \rightarrow 2H^*$	7.73×10^{-1}	0.939	0.0
R_{12}	$2H^* \rightarrow H_2 + 2*$	5.56×10^{11}	−0.435	$20.4 - 5\theta_H - 7.4\theta_{CO} + f(T)$
R_{13}	$OH^* + * \rightarrow H^* + O^*$	1.41×10^{11}	−0.375	$24.2 + f(\theta_O, \theta_H, \theta_{H_2O}, \theta_{CO}, T)$
R_{14}	$H^* + O^* \rightarrow OH^* + *$	1.73×10^{10}	−0.710	$14.2 + f(\theta_O, \theta_H, \theta_{H_2O}, \theta_{CO}, T)$
R_{15}	$H_2O^* + * \rightarrow H^* + OH^*$	7.58×10^{11} 3.79×10^{11} [c]	0.828	$15.4 + f(\theta_O, \theta_H, \theta_{OH}, \theta_{H_2O}, \theta_{CO}, T)$
R_{16}	$H^* + OH^* \rightarrow H_2O^* + *$	9.46×10^{10} 4.73×10^{10} [c]	0.498	$17.6 + f(\theta_O, \theta_H, \theta_{OH}, \theta_{H_2O}, \theta_{CO}, T)$
R_{17}	$H_2O^* + O^* \rightarrow 2OH^*$	1.87×10^{10}	−0.918	$11.4 + f(\theta_O, \theta_{OH}, \theta_{H_2O}, T)$
R_{18}	$2OH^* \rightarrow H_2O^* + O^*$	3.20×10^{10}	−1.485	$23.6 + f(\theta_O, \theta_{OH}, \theta_{H_2O}, T)$
R_{19}	$OH + * \rightarrow OH^*$	5.59×10^{-2}	0.354	0.0
R_{20}	$OH^* \rightarrow OH + *$	5.42×10^{13}	−1.593	$70 - 33\theta_O + 25\theta_{H_2O} + f(T)$
R_{21}	$H_2O + * \rightarrow H_2O^*$	7.72×10^{-2}	1.407	0.0
R_{22}	$H_2O^* \rightarrow H_2O + *$	2.06×10^{13}	−1.861	$10.8 - 4.5\theta_{H_2O} + 25\theta_{OH} + f(T)$
R_{23}	$H + * \rightarrow H^*$	1.63×10^{-1}	1.688	0.0
R_{24}	$H^* \rightarrow H + *$	2.83×10^{12}	1.164	$62.3 - 2.5\theta_H - 3.7\theta_{CO} + f(T)$
		Coupling between CO and H_2 chemistries on Rh		
R_{25}	$CO_2* + H^* \rightarrow CO^* + OH^*$	1.07×10^{11}	0.030	$4.4 + f(\theta_O, \theta_H, \theta_{H_2O}, \theta_{CO}, T)$
R_{26}	$CO^* + OH^* \rightarrow CO_2* + H^*$	9.38×10^{10}	−0.030	$20.5 + f(\theta_O, \theta_H, \theta_{H_2O}, \theta_{CO}, T)$
R_{27}	$COOH + * \rightarrow COOH^*$	1.51×10^{-2}	−0.938	0.0
R_{28}	$COOH^* \rightarrow COOH + *$	4.69×10^{13}	0.938	$62.2 + f(T)$
R_{29}	$COOH^* + * \rightarrow CO^* + OH^*$	4.83×10^{11}	−0.397	$6.2 + f(\theta_O, \theta_H, \theta_{H_2O}, \theta_{CO}, T)$
R_{30}	$CO^* + OH^* \rightarrow COOH^* + *$	2.07×10^{10}	0.397	$18.6 + f(\theta_O, \theta_H, \theta_{H_2O}, \theta_{CO}, T)$
R_{31}	$COOH^* + * \rightarrow CO_2* + H^*$	4.57×10^{11} 4.57×10^{10} [c]	−0.434	$4.2 + f(\theta_H, \theta_{CO}, T)$
R_{32}	$CO_2* + H^* \rightarrow COOH^* + *$	2.19×10^{10} 2.19×10^{9} [c]	0.434	$0.6 + f(\theta_H, \theta_{CO}, T)$
R_{33}	$CO^* + H_2O^* \rightarrow COOH^* + H^*$	7.15×10^{10}	0.440	$20.7 + f(\theta_H, \theta_{OH}, \theta_{H_2O}, \theta_{CO}, T)$
R_{34}	$COOH^* + H^* \rightarrow CO^* + H_2O^*$	1.40×10^{11}	−0.440	$10.5 + f(\theta_H, \theta_{OH}, \theta_{H_2O}, \theta_{CO}, T)$
R_{35}	$CO_2* + OH^* \rightarrow COOH^* + O^*$	9.54×10^{10}	0.200	$22.3 + f(\theta_O, \theta_{H_2O}, T)$
R_{36}	$COOH^* + O^* \rightarrow CO_2* + OH^*$	1.05×10^{11}	−0.200	$16.0 + f(\theta_O, \theta_{H_2O}, T)$
R_{37}	$CO_2* + H_2O^* \rightarrow COOH^* + OH^*$	7.44×10^{10}	0.479	$13.5 + f(\theta_O, \theta_{OH}, \theta_{H_2O}, T)$
R_{38}	$COOH^* + OH^* \rightarrow CO_2* + H_2O^*$	1.34×10^{11}	−0.479	$19.4 + f(\theta_O, \theta_{OH}, \theta_{H_2O}, T)$
R_{39}	$HCOO + 2* \rightarrow HCOO^{**}$	1.89×10^{-2}	−0.555	0.0
R_{40}	$HCOO^{**} \rightarrow HCOO + 2*$	3.74×10^{13}	0.555	$69.2 + f(T)$
R_{41}	$CO_2* + H^* \rightarrow HCOO^{**}$	1.40×10^{10}	0.654	$4.2 + f(\theta_H, \theta_{CO}, T)$
R_{42}	$HCOO^{**} \rightarrow CO_2* + H^*$	7.12×10^{11}	−0.654	$0.0 + f(\theta_H, \theta_{CO}, T)$
R_{43}	$CO_2* + OH^* + * \rightarrow HCOO^{**} + O^*$	5.97×10^{10}	0.431	$27.5 + f(\theta_O, \theta_{H_2O}, T)$
R_{44}	$HCOO^{**} + O^* \rightarrow CO_2* + OH^* + *$	1.67×10^{11}	−0.431	$13.4 + f(\theta_O, \theta_{H_2O}, T)$

(*continued on next page*)

Table 1 (*Continued*)

No.	Reaction	Sticking coefficient (unitless) or pre-factor (s^{-1})	Temperature exponent β	Activation energy at 300 K (kcal/mol)
R_{45}	$CO_2{}^* + H_2O^* + * \rightarrow HCOO^{**} + OH^*$	4.78×10^{10}	0.696	$18.4 + f(\theta_O, \theta_{OH}, \theta_{H_2O}, T)$
R_{46}	$HCOO^{**} + OH^* \rightarrow CO_2{}^* + H_2O^* + *$	2.09×10^{11}	−0.696	$16.4 + f(\theta_O, \theta_{OH}, \theta_{H_2O}, T)$

The activation energies are temperature dependent according to statistical mechanics (see Table 2) [1,17,18]. The modified Arrhenius expression,

$$k = \frac{A}{\sigma^{n-1}}\left(\frac{T}{T_0}\right)^{\beta} e^{-E/(R_g T)} \quad \text{or} \quad k = \frac{s}{\sigma^n}\sqrt{\frac{R_g T}{2\pi M}}\left(\frac{T}{T_0}\right)^{\beta} e^{-E/(R_g T)},$$

is used for computing the rate constant k. Here A is the pre-factor, s is the sticking coefficient, σ is the site density, n is the reaction order, β is the temperature exponent, E is activation energy, R_g is the ideal gas constant, and T is the absolute temperature. The coverage dependence of the activation energies of various reaction steps is incorporated in our simulations via the UBI-QEP method [37,38]. The functions f in the last column indicate the nonlinear dependence of activation energies on specific coverages indicated and on temperature.

[a] A bond index of 0.8 is used in the UBI-QEP formula for the calculation of the forward activation energy, instead of the usual value of 0.5.

[b] The backward activation energy is calculated using the forward activation energy of R_9 and the heat of reaction.

[c] Modified pre-factor to improve the predictions of the coupling mechanism against the CO PROX experiments of [53].

ing reaction mechanisms on Pt [13,14,19] and merely serve as starting values that are optimized against experimental data and thermodynamic constraints (see Section 2.3).

The adsorption steps are considered to be non-activated, in accordance with previous mechanisms in [3,5–10] and experiments on the specific diatomics [30,35]. Most chemisorption energies and adsorbate–adsorbate interactions are taken as intermediate values from a range of literature experimental and DFT data without further adjustment. Hydrogen bonding interactions of 25 kcal/(mol ML) (ML stands for monolayer) are assumed between adsorbed OH and H_2O molecules, by analogy to Pt [1], based on the DFT calculations of Michaelides and Hu [36]. The species chemisorption energies and their coverage dependence are summarized in Table 2.

These coverage-dependent heats of chemisorption, shown in Table 2, are then used in the UBI-QEP framework [37,38] to calculate the activation energies of the reaction steps. The activation energies are shown in Table 1. For the LH surface reaction R_9–R_{10} ($CO_2{}^* + * \leftrightarrow CO^* + O^*$), we propose a modified bond index of 0.8 instead of the UBI-QEP value of 0.5 that is usually assumed [37,38]. Such modification was previously proposed for CO oxidation on Pt [18], because of a comparison of the UBI-QEP estimate with DFT pre-

Table 2
Temperature and coverage dependent heats of chemisorption using statistical mechanics [1,17,18] and the UBI-QEP method [37,38]. The heat of chemisorption, $Q(T)$, decreases with increasing temperature (here $\Delta T = T - T_0$ and $T_0 = 300$ K)

Species	Heat of chemisorption Q (kcal/mole)	References	Temperature dependence[a] $\frac{Q(T_0)-Q(T)}{R_g \Delta T}$	Changes in degrees of freedom for deriving the temperature dependence[b]
O^*	$100 - 21\theta_O$	Expts. [28,59,60], DFT [61–63]	1.5	$-3F_T + 3F_V$
CO^*	$38.5 - 17\theta_{CO} - 3.7\theta_H$	Expts. [34,64–66], DFT [67,68], our DFT calculations	2.0	$-3F_T - 2F_R + F_{RR} + 4F_V$
$CO_2{}^*$	5.2	Expts. [69,70], UBI-QEP [71]	2.0	$-F_T - 3F_R + 4F_V$
H^*	$62.3 - 2.5\theta_H - 3.7\theta_{CO}$	Expts. [31], DFT [61,72–74], our DFT calculations	1.5	$-3F_T + 3F_V$
OH^*	$70 - 33\theta_O + 25\theta_{H_2O}$	UBI-QEP [71], DFT [61,73]	2.0	$-3F_T - 2F_R + F_{RR} + 4F_V$
H_2O^*	$10.8 - 4.5\theta_{H_2O} + 25\theta_{OH}$	Expts. [75], DFT [61,76]	2.5	$-3F_T - 3F_R + F_{RR} + 5F_V$
$COOH^*$	62.2	DFT [56]	2.5	$-3F_T - 3F_R + F_{RR} + 5F_V$
$HCOO^{**}$ (bidentate)	69.2	DFT [56]	3.0	$-3F_T - 3F_R + 6F_V$

[a] The generalized assumptions to calculate the temperature dependence are as follows: (1) Each translational, rotational, and vibrational degree of freedom (DOF) corresponds to $0.5R_gT$, $0.5R_gT$, and R_gT, respectively, where R_g is the universal gas constant. (2) Upon adsorption, all translational DOF are converted into vibrational DOF. In the case of weakly bound molecules (such as CO_2), only 1 translational DOF is lost upon adsorption (the molecule is able to move readily on the surface). (3) All rotational DOF are converted into vibrational DOF upon adsorption. For species, such as OH^*, H_2O^*, and $COOH^*$, with a vertical axis through the adsorbed atom, 1 of the gained vibrational DOF is assumed to be a free, internal rotor (rigid rotor approximation) and counts as $0.5R_gT$.

[b] F_T, F_R, and F_V stand for translational, rotational, and vibrational DOF. F_{RR} indicates that a vibrational DOF is assumed to be a free, internal rotor. The 'minus' and 'plus' signs indicate loss and gain of DOF, respectively.

dictions and experimental data. This modification is further supported by recent DFT work [39–43], which shows that for certain classes of reactions, the structure of the transition state is more similar to the products than the reactants or vice versa. As an example, Michaelides et al. [39] found that dissociation activation energies are typically linearly proportional to the heats of reaction with a slope of 0.86, rather than the classical value of 0.5; this high slope implies that these surface reactions have product-like or late transition states. This is an example of how semiempirical methods can be improved or retained based on higher level theoretical (DFT) tools.

The last part of parameter estimation is associated with ensuring enthalpic consistency as the temperature varies, following the concepts discussed in [17]. Briefly, the gas-phase reaction enthalpies are temperature dependent. To ensure enthalpic consistency in a mechanism, the enthalpies of adsorption, desorption, and surface reactions should also be temperature dependent. We use statistical mechanics to incorporate temperature dependence in the heats of chemisorption by accounting for the changes in translational, rotational, and vibrational degrees of freedom (DOF) that occur upon adsorption–desorption [1,17,18]. For example, O has three translational DOF in gas phase. It is assumed that upon adsorption, these DOF are converted into three vibrational DOF. Assuming each translational DOF and vibrational DOF to be approximately equal to $0.5R_gT$ and R_gT, respectively, the net heat of chemisorption has a temperature dependence of $1.5R_gT$. Here, R_g is the universal gas constant and T is the temperature. Note that different assumptions may be invoked. For example, one could account for the high mobility of certain species, such as H, on the surface at higher temperatures. However, heats of chemisorption change moderately over typical temperature ranges. The temperature dependence of the heats of chemisorption and the associated formulae are summarized in Table 2. Since heats of chemisorption are input to the UBI-QEP method to compute activation energies, this temperature dependence makes the activation energies also temperature dependent. Ensuring entropic consistency as a function of temperature is also crucial, and this is achieved in the optimization process with a previously described method [17]. In the remainder of the paper, no adjustment of the activation energies is made.

Figs. 1–4 show the predictions (dashed lines) made with the screening mechanisms against experimental data for CO ignition [24], molecular beam CO oxidation [25], H_2 ignition (this work), and LIF H_2/O_2 experiments [5], respectively. Predictions are qualitative, indicating that the mechanisms and associated parameters are reasonable. However, the agreement between model predictions and the experimental data is not spectacular. In particular, the ignition temperatures are either underpredicted (for CO in Fig. 1) or overpredicted (for H_2 in Fig. 3). Reaction rate predictions in Fig. 2 are flatter compared with the experimental data, whereas the slope in the LIF predictions in Fig. 4 is not in complete agreement with the experimental data.

2.3. Optimization of pre-factors, model predictions, and validation

Predictions made with the screening mechanisms are not quantitative. This is due in part to the fact that the initial pre-factor and sticking coefficient estimates are very crude and do not obey entropic consistency. Optimization and enforcement of entropic consistency of these parameters are therefore necessary. To reduce the number of parameters optimized, neither heats of chemisorption nor activation energies are modified. SA is first carried out to select targeted experiments for optimization, as described in Appendix A. The experimental data in Figs. 1–4 have been selected as optimization targets, and other data, judged as providing redundant information in terms of the key kinetic parameters, are left for validation (see Appendix B). Note that these data are collected on single crystal, polycrystalline foil and supported catalysts and over a range of pressures. This diversity is due in part to a lack of such data on the same (e.g., supported) catalyst and in part is created purposely to overcome the materials and pressure gaps. Obviously, it is tacitly assumed that the fundamental chemistry is structure insensitive.

The optimization range for sticking coefficients is taken to be 5×10^{-3} to 1 (see [44,45] for typical estimates), whereas that for pre-factors is taken to be as two orders of magnitude in either direction from the nominal values mentioned above. The sticking coefficient of CO is restricted to the range of 0.5–1, based on typical values reported in [46–48]. To ensure entropic consistency, the implicit thermodynamic constraints approach with a modified Arrhenius equation (denoted as case b in [17]) is used in the optimization. The IMSL subroutine library [49] is used for optimization.

The screening CO mechanism is first optimized against the CO ignition [24] and the molecular beam CO oxidation [25] experiments. While the screening H_2 mechanism is optimized against the H_2 ignition (this work) and the LIF H_2 oxidation [5] experiments, the oxygen parameters (common reactions R_1–R_4) are kept the same as those in the optimized CO oxidation mechanism. Pre-factors and temperature exponents of both mechanisms are optimized against experimental points, along with entropic constraints over a temperature range from room temperature to ∼2000 K. The optimized parameters are shown in Table 1. The mechanisms in Table 1 are hereafter referred to as the *optimized* CO and H_2 oxidation mechanisms.

Predictions using the optimized parameters against the targeted experiments are shown in Figs. 1–4 (solid lines), where reasonably good performance is observed. Significant improvement in thermodynamic consistency is observed after optimization (ratios of equilibrium constants lie close to 1) compared with the screening mechanisms (ratios of equilibrium constants are on the order of 10^2–10^3), over the temperature range of 300–2000 K. Further validation of

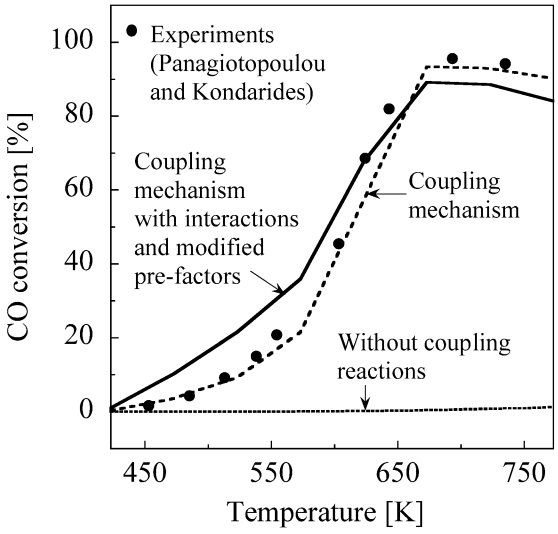

Fig. 5. Predictions of the coupling mechanism (R_1–R_{46}) against the WGS experimental data of [50]. The operating conditions include a pressure of 1 atm, a reactor volume of ∼0.5 cm^3, an inlet flow rate of 200 cm^3/min, and an inlet composition of 3% CO, 10% H_2O, and 87% N_2. A/V is fitted to 13.7 cm^{-1}. Predictions without coupling reactions, i.e., with only reactions R_1–R_{24} of Table 1, are also shown with dotted lines.

these mechanisms against additional experimental data sets is shown in Appendix B.

3. Development of a CO–H_2 coupling mechanism

3.1. Experimental data on WGS and CO PROX on Rh

Interest in WGS and CO PROX on noble metals has recently increased because of their non-pyrophoric nature and high activity in the presence of steam. Different research groups have used Rh for such experiments. Panagiotopoulou and Kondarides [50] carried out fixed-bed WGS experiments on Rh/TiO_2 and found that Rh is an active catalyst for WGS (Fig. 5). Wheeler et al. [51] and Utaka et al. [52] carried out WGS experiments with a Rh/Al_2O_3 washcoat monolith reactor and a fixed-bed reactor with Rh/Al_2O_3 catalyst, respectively, and found similar observations. In those experiments, CO conversion initially increases as a function of temperature, corresponding to a kinetically controlled regime, and then decreases at higher temperatures because of the reverse water–gas shift (RWGS) reaction.

Regarding CO PROX experiments, Han et al. [53] measured CO conversion and selectivity on a Rh/MgO catalyst in a fixed-bed microreactor. Similar to WGS, the CO conversion shows a maximum, whereas the selectivity for CO oxidation significantly decreases from ∼70 to ∼30% (Fig. 6). Ito et al. [54] studied the low-temperature regime of CO PROX (80–140 °C) on Rh/SiO_2 and observed a continuous rise in CO conversion with increasing temperature (Fig. B.7). Chen et al. [55] studied the effect of inlet composition on CO conversion in a microchannel reactor (Fig. B.8).

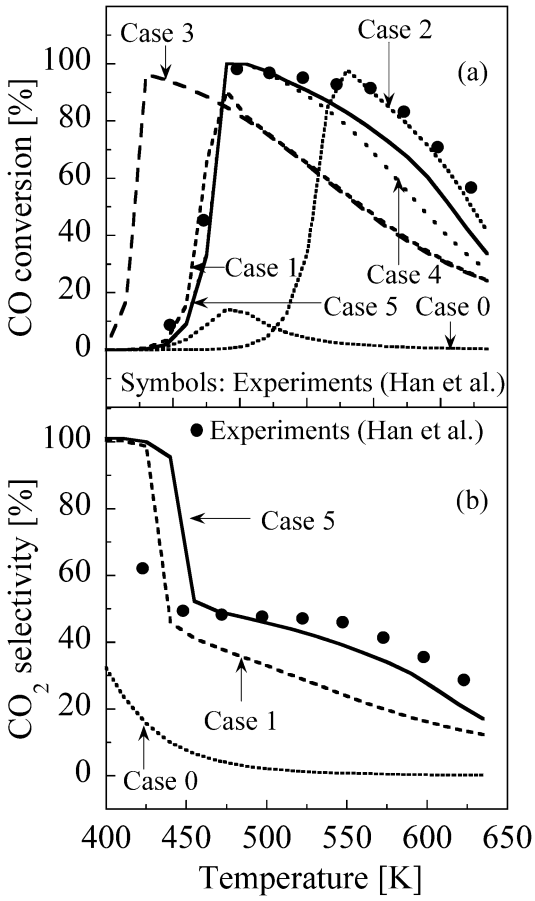

Fig. 6. Predictions of the coupling mechanism against the CO PROX experimental data of [53]. The operating conditions include a pressure of 1 atm, a reactor volume of ∼0.1 cm^3, an inlet flow rate of 120 cm^3/min at STP, and an inlet composition of 1% CO, 1% O_2, 75% H_2, and 23% N_2. Five different cases are shown with the coupling mechanism, viz., (1) $A/V = 3.5 \times 10^5$ cm^{-1}, (2) $A/V = 600$ cm^{-1}, (3) $A/V = 3.5 \times 10^5$ cm^{-1} and CO–H interactions of 3.7 kcal/(mol ML), (4) $A/V = 600$ cm^{-1} and CO–H interactions of 3.7 kcal/(mol ML), and (5) $A/V = 600$ cm^{-1}, CO–H interactions of 3.7 kcal/(mol ML), and modified pre-factors (shown in italics in Table 1). Case 0 represents predictions without the coupling reactions, i.e., with only reactions R_1–R_{24} of Table 1, with an A/V of 3.5×10^5 cm^{-1}.

These different types of experiments cover a wide range of operating conditions and are useful in the optimization and validation of the surface reaction mechanism.

3.2. Coupling pathways, initial parameter estimation, and predictions

For the combined reaction steps (R_1–R_{24}) of the CO and H_2 combustion mechanisms, little activity is found under typical WGS and PROX experimental conditions, as shown in Figs. 5 and 6, respectively. In this mechanism, the oxidation of CO^* occurs via O^* forming by dissociative adsorption of O_2 in the case of PROX or after complete dissociation of H_2O^* in the case of WGS

$$H_2O^* \rightarrow OH^* + H^* \rightarrow O^* + 2H^*. \quad (3)$$

In our previous work on WGS and PROX on Pt, we showed that aside from the obvious coupling of site competition between the two fuels and sharing of O^* as an oxidant, there are additional chemical reaction steps that couple the two reaction mechanisms [1]. These coupling steps between CO and H_2 chemistries are essential for providing sufficient speed to capture the promoting effect of water on CO oxidation as well as WGS and PROX experimental data, even under equilibrium conditions, with reasonable catalyst surface areas [1].

Here we propose the same additional mechanistic steps for Rh (R_{25}–R_{46}), shown in Table 1. The coupling pathways include the oxidation of adsorbed carbon monoxide CO^* by OH^* to $CO_2{}^*$ via the direct path R_{26}

$$CO_2{}^* + H^* \leftrightarrow CO^* + OH^*. \qquad (R_{25}–R_{26})$$

The indirect oxidation CO^* to $CO_2{}^*$ by OH^* via path R_{30} entails the intermediate carboxyl $COOH^*$ formation and thermal decomposition:

$$COOH^* + {}^* \leftrightarrow CO^* + OH^*, \qquad (R_{29}–R_{30})$$

$$COOH^* + {}^* \leftrightarrow CO_2{}^* + H^*, \qquad (R_{31}–R_{32})$$

and the oxidation of CO^* by H_2O^* (reaction R_{33}),

$$CO^* + H_2O^* \leftrightarrow COOH^* + H^*. \qquad (R_{33}–R_{34})$$

Additional $COOH^*$-related reactions (R_{27}–R_{28} and R_{35}–R_{38}, which describe other steps to $CO_2{}^*$ from carboxyl) and formate ($HCOO^{**}$)-related steps (R_{39}–R_{46}) are also accounted for. The overall mechanism in Table 1 (R_1–R_{46}) is referred to as the *coupling mechanism*.

The heats of chemisorption of $COOH^*$ and $HCOO^{**}$ are taken from [56]. Pre-factors and activation energies are estimated with the same approach explained in Section 2. The pre-factors and sticking coefficients are made thermodynamically consistent by minimizing of the deviation between gas-phase reaction entropies and surface reaction entropies (see [1] for details). The thermodynamically consistent parameters of the coupling mechanism are shown in Table 1, and the relevant heats of chemisorption and their statistical mechanics-based temperature dependence are shown in Table 2.

The coupling mechanism is used to model the WGS and CO PROX experiments of [50] and [53], respectively, without any adjustments of kinetic parameters. With the area of catalyst per unit reactor volume (A/V) as an adjustable parameter, it is possible to get reasonable agreement with the experimental WGS data, as shown in Fig. 5 (dashed lines). Even though the WGS data are captured well, the CO conversion and selectivity in PROX are substantially underpredicted at high temperatures (case 1 in Fig. 6). Furthermore, the good agreement at low temperatures of PROX is only possible for an A/V value of $> 10^5 \mathrm{cm}^{-1}$ that is too high. Therefore, it is necessary to resolve this issue.

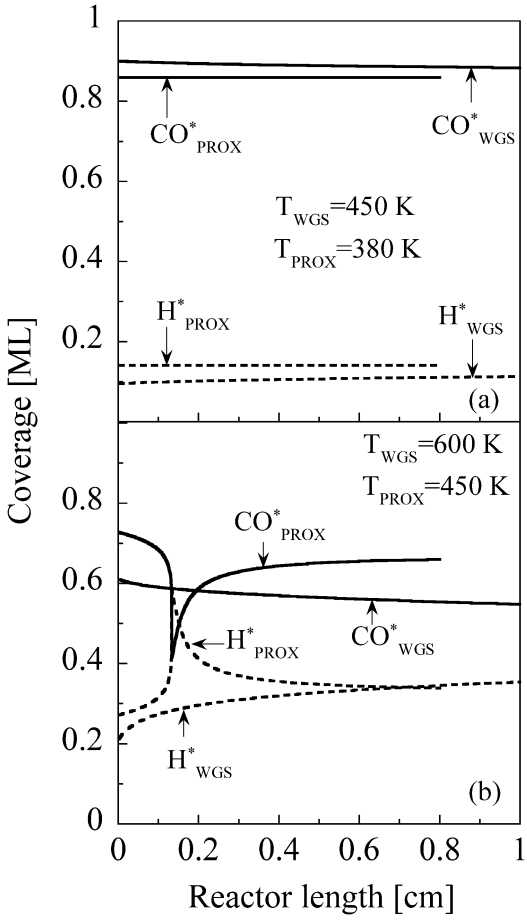

Fig. 7. Dominant surface species coverage profiles under typical WGS and PROX conditions, using the coupling mechanism without CO–H interactions or any pre-factor modification. Panels a and b correspond to low and high temperatures, respectively.

3.3. Hierarchical multiscale parameter refinement using DFT

As a first step toward rationalizing the inability of the coupling mechanism to predict the PROX data, the coverages of dominant surface species are checked. Under the low temperatures of WGS and PROX, CO^* and H^* are the most abundant reactive intermediates (MARI), with coverages on the order of 0.9 and 0.1, respectively, as shown in Fig. 7a. At high temperatures, the CO^* and H^* coverages are in the range of 0.4–0.7 and 0.2–0.5, respectively (e.g., see Fig. 7b). Whereas the heats of chemisorption account for CO–CO and H–H interactions, adsorbate–adsorbate interactions between CO^* and H^* need to be incorporated into the kinetic parameters, given that both species are present in significant fractions on the surface. This is an example of hierarchical multiscale parameter refinement, whose overall idea was discussed in [21] and relies on refinement of parameters of the semiempirical UBI-QEP method using DFT calculations, only after the simulations have been carried out with the semiempirical method to identify the MARI and rate-determining steps.

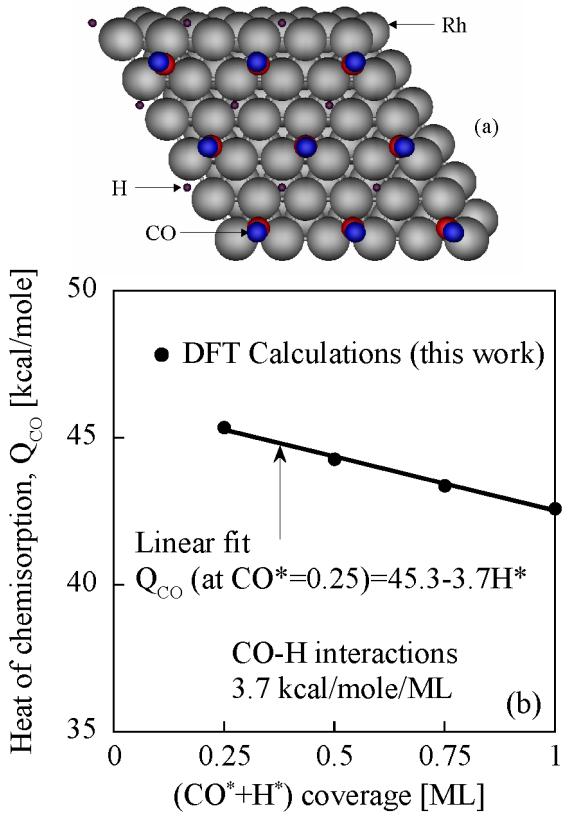

Fig. 8. Panel (a) shows the Rh slab with CO and H atoms, corresponding to a H^*-coverage of 0.25 ML and a CO^* coverage of 0.25 ml. A (2×2) periodic unit cell is used. Panel b shows the heat of CO chemisorption versus H^*-coverage ($\theta_{CO} = 0.25$) using DFT calculations on a three-layer Rh(111) slab. The line in panel (b) is a linear fit to the calculation points. Repulsive CO–H interactions of ∼3.7 kcal/(mol ML) are found.

We have carried out periodic DFT calculations on a three-layer 2×2 Rh(111) slab with DACAPO software [57]. A total of eight DFT calculations, that is, gas-phase CO, gas-phase H, Rh slab, CO/Rh, H/Rh, (CO + H)/Rh, (CO + 2H)/Rh, and (CO + 3H)/Rh, are carried out. The adsorbates and the top two slab layers are relaxed, whereas the bottom slab layer is fixed. A picture of adsorbates on the Rh slab is shown in Fig. 8a. Fig. 8b shows the effect of H^* coverage on the heat of CO chemisorption. Repulsive CO–H interactions of 3.7 kcal/(mol ML) are found. While calculating these interactions, we assumed pairwise additivity. Upon the addition of an H to a system of $CO + nH$ ($n = 0, 1, 2$), CO–H and H–H interactions are estimated. Furthermore, it is assumed that the effect of CO on H is the same as that of H on CO. Because of symmetry and a typically observed linear behavior for other systems [21,58], a similar dependence of the heat of H chemisorption on CO^* coverage is assumed (see Table 2). Even though the magnitude of these interactions is relatively small, these cross-interactions significantly affect the H_2 desorption energy (by as much as ∼7 kcal/mol, which is a ∼35% decrease compared with the zero coverage desorption energy of ∼20 kcal/mol). Such a substantial decrease in activation energy of desorption results in a decrease in H^* coverage due to the high CO^* coverage, and a further increase in the CO^* coverage toward 1, which in turn changes the mechanism activity at these relatively low temperatures. In comparison, since the H^* coverage is small, the CO desorption energy is less affected (see Table 2). This coverage dependence is then incorporated into the UBI-QEP method and affects a number of reaction steps.

In the WGS reaction, without CO-H interactions, the reaction

$$CO^* + H_2O^* \leftrightarrow COOH^* + H^* \qquad (R_{33}–R_{34})$$

is the most dominant CO consumption reaction at low temperatures (e.g., 450 K). When CO–H interactions are included, the H_2 desorption energy decreases, leading to a higher CO^* coverage. Because of an order-of-magnitude decrease in H^*-coverage, all remaining coverages, including H_2O^*, increase. At the same time, the activation energy of R_{33} increases slightly, leading to an overall increase in the rate of R_{33} by a factor of ∼2. Therefore, the CO–H interactions shift the activity to lower temperatures (not shown) by ∼50 °C, but the dominant CO consumption pathway remains the same at low temperatures. Overall, the cross-CO–H interactions accelerate the onset of catalyst activity, but their effect is not dramatic.

In the PROX reaction, without the CO–H interactions, both R_{10},

$$CO^* + O^* \rightarrow CO_2{}^* + {}^* \qquad (R_{10})$$

and the carboxyl path R_{30},

$$CO^* + OH^* \rightarrow COOH^* + {}^* \qquad (R_{30})$$

are the important CO consumption pathways at low temperatures. The CO–H interactions decrease the H_2 desorption energy by ∼7 kcal/mol, resulting in an increase of the CO^* coverage of up to ∼0.96 at low temperatures (e.g., at 380 K) and a reduction of H^* coverage. The activation energy of hydroxyl formation,

$$H^* + O^* \rightarrow OH^* + {}^* \qquad (R_{14})$$

decreases by ∼2 kcal/mol, resulting in higher OH^* production. This increased rate of OH^* production, in conjunction with a similar decrease in the activation energy of the carboxyl formation via R_{30} by ∼1.5 kcal/mol, gives rise to a higher rate of R_{30}. The net result is that R_{30} becomes the most dominant CO consumption reaction and leads to higher CO conversion at lower temperatures without the need for unrealistically high surface areas. Overall, the CO–H interactions shift the activity to lower temperatures (case 3 in Fig. 6a) by ∼50 °C when A/V is kept fixed. However, the high-temperature data are still not well captured. An important consequence of including interactions is that one can now adjust A/V to a reasonable value to predict the low-temperature region and part of the high-temperature data fairly well (case 4 in Fig. 6a). With this moderate A/V, when the interactions are turned off, the low-temperature activity drops (case 2 in Fig. 6a). Therefore, in PROX the

CO–H interactions significantly affect the dominant CO consumption pathways at low temperatures and enhance the net rate for CO consumption.

The effect of CO–H lateral adsorbate–adsorbate interactions on chemistry is an additional manifestation of synergism between multiple fuels arising from concentration or proximity effects, that is, the fact that surface processes often operate under non-dilute and therefore non-ideal conditions. This coupling is unique to reactions in liquids and on surfaces. In our case, the presence of CO at low temperatures has a promoting effect on CO combustion, with hydrogen used to combust and regenerate H^*.

Reaction path analysis (RPA) at 380 K shows that reactions R_{14} ($H^* + O^* \rightarrow OH^* + {}^*$) and R_{10} ($CO^* + O^* \rightarrow CO_2{}^* + {}^*$) contribute equally to O^* consumption without CO–H interactions. CO^* consumption occurs almost equally through R_{10} and R_{30} ($CO^* + OH^* \rightarrow COOH^* + {}^*$), as mentioned before. Furthermore, R_{16} ($H^* + OH^* \rightarrow H_2O^* + {}^*$) is negligible compared with R_{14}. This results in *a H^*-catalyzed path*, given as

$$H^* + O^* \rightarrow OH^* + {}^*, \qquad (R_{14})$$

$$CO^* + OH^* \rightarrow COOH^* + {}^*, \qquad (R_{30})$$

$$COOH^* + {}^* \rightarrow CO_2{}^* + H^*, \qquad (R_{31})$$

$$\text{net:} \quad CO^* + O^* \rightarrow CO_2{}^* + {}^*, \qquad (R_{31})$$

where no net consumption of H^* occurs, giving rise to 100% CO_2 selectivity. However, with CO–H interactions, the activation energy of R_{16} decreases by ∼1.9 kcal/mol, leading to $R_{14} \approx R_{16}$. Since R_{16} is no longer negligible, some net H_2 consumption occurs, leading to a moderate selectivity for CO_2 formation.

3.4. Important reactions for PROX at high temperatures

By including CO–H interactions, the coupling mechanism still underpredicts the highest temperature PROX data (case 4 in Fig. 6a). To improve the high-temperature predictions, a pairwise SA is carried out at high temperatures (635 K) with respect to the pre-factors. The forward and backward pre-factors are perturbed by the same fraction to maintain thermodynamic consistency. SA indicated (not shown here) that the water dissociation reaction,

$$H_2O^* + {}^* \leftrightarrow H^* + OH^* \qquad (R_{15}\text{–}R_{16})$$

is the most important step (normalized sensitivity coefficient $= -0.28$), followed by the carboxyl decomposition reaction,

$$COOH^* + {}^* \leftrightarrow CO_2{}^* + H^* \qquad (R_{31}\text{–}R_{32})$$

(normalized sensitivity coefficient $= -0.05$). To keep the predictions of optimized H_2 mechanism nearly unaltered, we decreased the pre-factors of R_{15}–R_{16} by a factor of only 2. The pre-factors of R_{31}–R_{32} are decreased by a factor of 10 to improve the high-temperature PROX predictions. This is another example of iterative parameter refinement. The modified pre-factors of these two steps are shown in Table 1 in italics. The predictions of the coupling mechanism with modified pre-factors are shown in Figs. 5 and 6 (solid lines, denoted as case 5 in Fig. 6). Both sets of data are fairly well captured, and the agreement at high temperature is significantly improved, especially for PROX. The WGS predictions in Fig. 5 are slightly deteriorated, but this is definitely outweighed by the significant gain in the PROX predictions in Figs. 6, B.7, and B.8. No adjustment of pre-factors was made for the WGS data. In the remainder of the paper, we refer to this set of parameters as *coupling mechanism with interactions and modified pre-factors*.

The results of the H_2 oxidation mechanism are almost unaffected by the pre-factor modification. Such pre-factor modification is within the range of uncertainty of typical parameter estimation techniques. In fact, instead of a change in the pre-factors of R_{31}–R_{32} by a factor of 10, an increase in the forward and backward activation energies by ∼2.5 kcal/mol (this could be done, for example, by a change in the bond index of these reactions from 0.5 to 0.8) gives similar predictions.

The CO–H interactions are also found to be important for providing sufficient activity for the PROX predictions shown in Figs. B.8 against the experimental data of [55]. Similarly, CO–H interactions are necessary to enable use of a moderate A/V value against the experimental PROX data of [54], as shown in Fig. B.7.

Finally, one should note that the dominant surface species are still CO^* (coverage ≈ 0.2–1.0) and H^* (coverage ≈ 0–0.8), for the coupling mechanism with CO–H interactions and modified pre-factors, which indicates that no further hierarchical parameter refinement is necessary in terms of additional adsorbate–adsorbate interactions.

3.5. Analysis of reaction pathways in the coupling mechanism with interactions and modified pre-factors

An RPA is carried out with the coupling mechanism with interactions and modified pre-factors, and adjusted A/V values to identify the important CO consumption paths as a function of temperature. Figs. 9a and b show the RPA for WGS and PROX, respectively. Figs. 10a and b compare the activation energies for the CO consumption pathways for typical WGS and PROX conditions, respectively, with adsorbate–adsorbate interactions taken into account (solid lines), and without interactions (dashed lines). R_{30} has the lowest activation energy with or without any adsorbate-adsorbate interactions between CO–CO, H–H, and CO–H. The interactions substantially decrease the activation energy of R_{30}.

At low temperatures, the dominant pathway for CO consumption in WGS is carboxyl formation by H_2O^*

$$CO^* + H_2O^* \rightarrow COOH^* + H^*. \qquad (R_{33})$$

However, at higher temperatures, the dominant CO consumption path changes to

$$CO^* + OH^* \rightarrow COOH^* + {}^*. \qquad (R_{30})$$

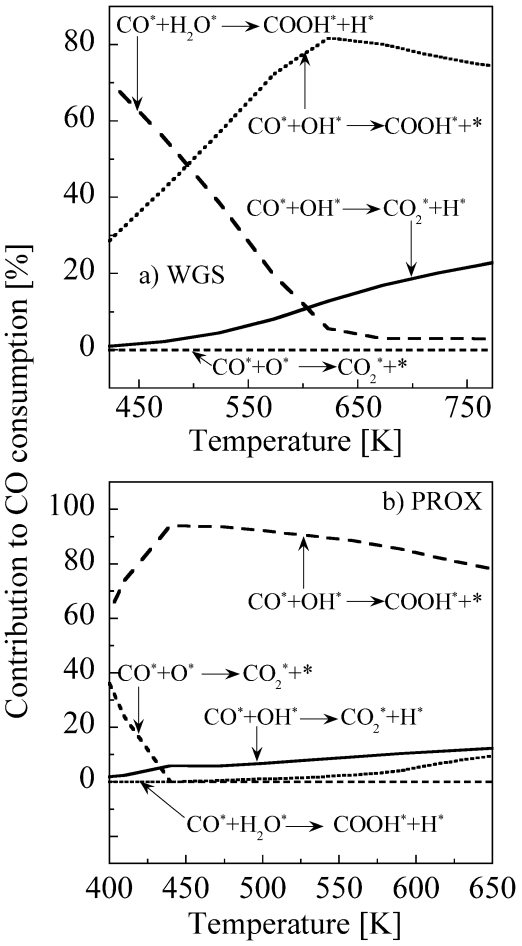

Fig. 9. RPA for WGS (a) and PROX (b) using the coupling mechanism with modified pre-factors and modified A/V values in the simulations. Various CO consumption pathways are analyzed excluding CO desorption, which has a significantly higher rate than the other reactions. A crossover in the dominant CO consumption pathway occurs for WGS as temperature increases.

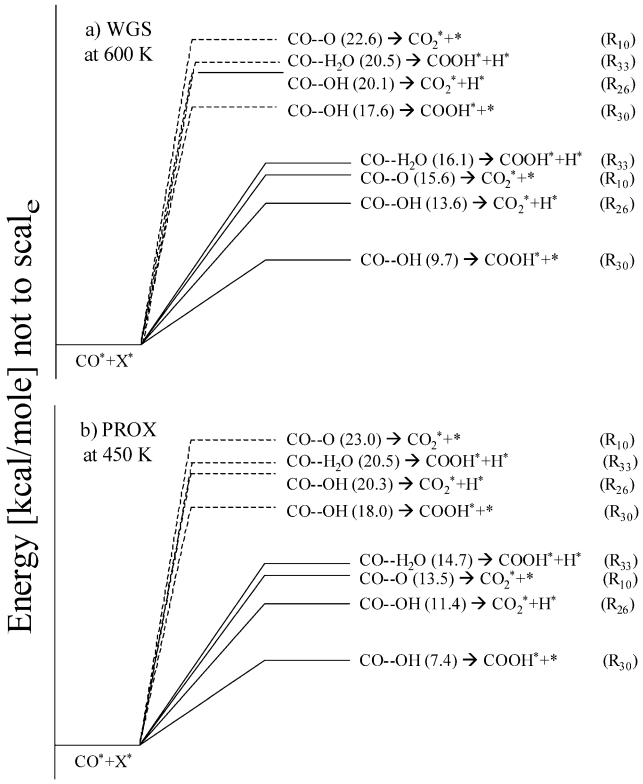

Fig. 10. Comparison of activation energies of various CO consumption reactions under typical WGS (a) and PROX (b) conditions. X^* indicates possible reactant, such as O^*, OH^*, or H_2O^*. Dashed lines indicate the energetics with no adsorbate-adsorbate interactions between CO–CO, H–H, or CO–H, whereas solid lines indicate coverage dependent activation energies. The values in parenthesis indicate the activation energy of a surface reaction. Typical coverages of CO^* and H^* are 0.6 and 0.15 for WGS at 600 K and 0.8 and 0.19 for PROX at 450 K. Reaction R_{30} ($CO^* + OH^* \rightarrow COOH^* + {}^*$) has the lowest activation energy under all conditions.

R_{30} has a lower activation energy than R_{33} at low temperatures (e.g., 5.7 kcal/mol vs. 13.6 kcal/mol at 450 K (not shown)) as well as at high temperatures (e.g., 9.7 kcal/mol vs. 16.1 kcal/mol at 600 K, as shown in Fig. 10a). However, at low temperatures, the OH^* coverage ($\sim 10^{-7}$) is negligible compared with that of H_2O^* ($\sim 10^{-4}$). Therefore, R_{33} dominates at low temperatures. On the other hand, at high temperatures, R_{33} and the H_2O^* decomposition reaction

$$H_2O^* + {}^* \rightarrow H^* + OH^* \qquad (R_{15})$$

with a comparable activation energy of 16.9 kcal/mol, start competing with the H_2O^* consumption path. As a result, more OH^* is produced at a coverage on the order of $\sim 10^{-5}$, and the rates of R_{30} and R_{26} ($CO^* + OH^* \rightarrow CO_2{}^* + H^*$) increase. Since the activation energy of R_{30} is much lower than that of R_{33}, there is a gradual crossover in the most important CO consumption pathway toward R_{30}. This crossover is different from our previous observations on Pt, where the carboxyl path R_{33} via H_2O^* dominated in the entire temperature range of WGS [20]. This is not an effect of CO–H interactions or pre-factor modification, because even without taking these into account, a similar crossover is mechanistically observed on Rh. As a final note, it is clear that activation energies alone (Fig. 10a) do not explain the dominant paths shown in Fig. 9a. Coverages are also important in controlling activation energies and the actual reaction rates via mass action kinetics.

In PROX on Rh, since H_2O^* coverage is negligible at the conditions of these experiments, R_{30} is the most dominant CO consumption pathway at all temperatures. This is again different from our observations on Pt [20], where all CO consumption paths (R_{26}, R_{30}, and R_{33}) except R_{24} contribute in different temperature ranges. Since the coupling mechanism on Rh shows higher CO conversion at all temperatures than the coupling mechanism on Pt [20], Rh is a better PROX catalyst than Pt, in accordance with the experiments of [53].

4. Conclusions

Toward the goal of developing a comprehensive surface reaction mechanism for natural gas partial oxidation on Rh

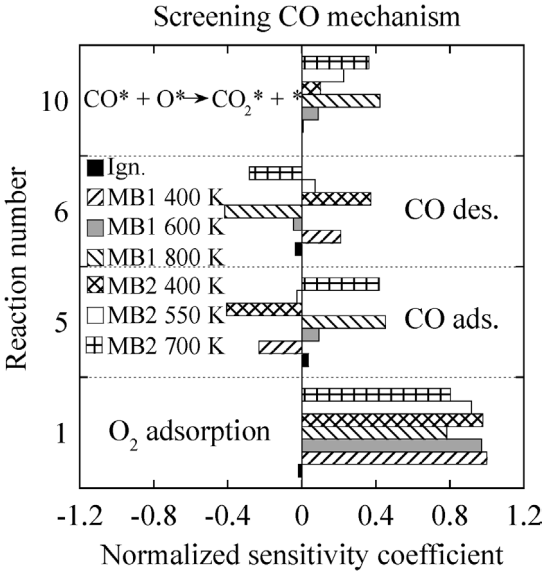

Fig. A.1. Sensitivity analysis (SA) of the screening CO mechanism against ignition (Ign.) data of [24] and molecular-beam (MB1 [25] and MB2 [26]) experiments at different temperatures.

and subsequent CO removal, thermodynamically consistent reaction sets have been proposed for CO and H_2 oxidation chemistry, WGS, and PROX reactions. Parameter estimation entailed combining the semiempirical UBI-QEP method, DFT calculations, and crude TST estimates. All reaction sets have been thermodynamically consistent from room temperature to ∼2000 K using statistical mechanics and constraints-based optimization. It has been found that the CO + O reaction in WGS and PROX reactions is slow, and additional CO–H_2 coupling reactions, including the carboxyl and hydroxyl intermediates as well as H_2O, are crucial steps for these processes. Incorporation of adsorbate–adsorbate CO–H interactions, computed via DFT, into the UBI-QEP semiempirical method in a hierarchical multiscale manner was found to be essential in developing a reaction mechanism that can predict the PROX data well. The proposed mechanisms capture targeted and additional experimental data well over a range of conditions. Their integration into methane and oxygenate chemistry will be discussed in a forthcoming publication. It is important to note that a one-step reduced-rate expression based on microkinetic models, such as that developed in [20], could be valuable for reactor design. Finally, identification of rate-determining step(s) could assist the improvement of catalysts.

Acknowledgments

This work was supported in part by ConocoPhillips and by the donors of the Petroleum Research Fund, administered by the American Chemical Society. ABM acknowledges Dr. Daniel Norton of University of Delaware for the assistance with the H_2 ignition studies in a microreactor. We also acknowledge Prof. Manos Mavrikakis of the University of Wisconsin, Madison, for providing heats of chemisorption data, used in Table 2, before publication.

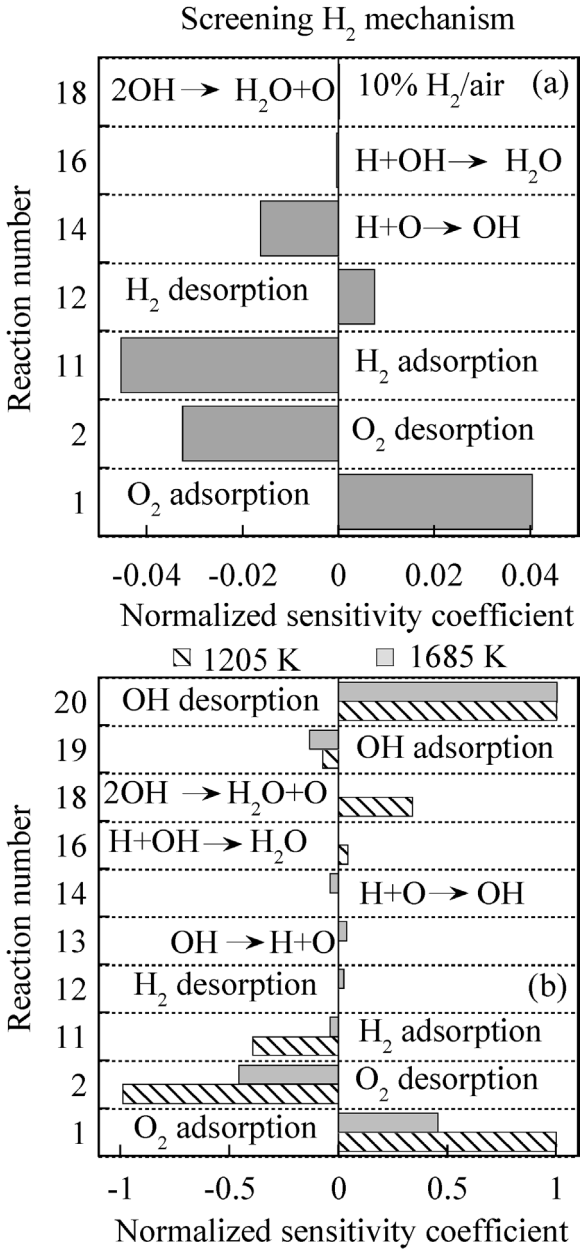

Fig. A.2. Sensitivity analysis (SA) of the screening H_2 mechanism for our ignition experiments at 10% H_2/air conditions (a) and LIF experiments of [5] at low and high temperatures (b).

Appendix A. Selection of targeted experiments for optimization of CO and H_2 screening mechanisms

Given multiple experimental data sets, one needs to select targeted experiments for optimization and regard other data sets as redundant experiments to validate the performance of an optimized mechanism. SA is a useful tool for such a task.

Fig. A.1 shows the SA of the screening CO mechanism for ignition (Ign.) data [24] and molecular-beam experiments

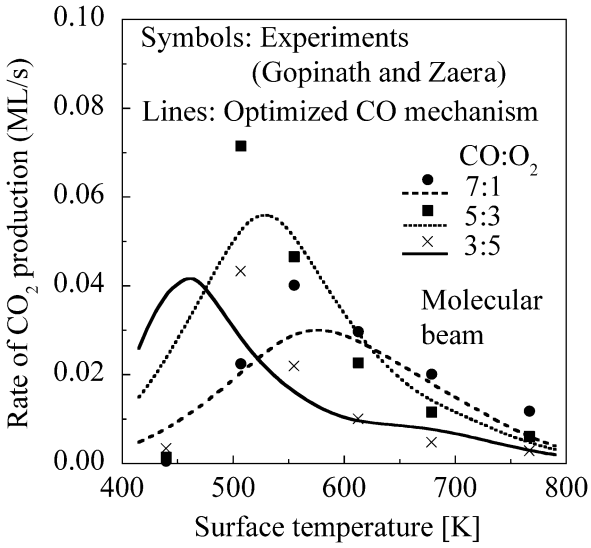

Fig. B.1. Assessment of the optimized CO mechanism against the molecular-beam experiments of [25] for different compositions of CO and O_2. The operating conditions include a total flux of 1 ML/s and CO/O_2 ratios of 7/1, 5/3, and 3/5. The experimental data is fairly well captured by the optimized mechanism. No fitting of these data is done.

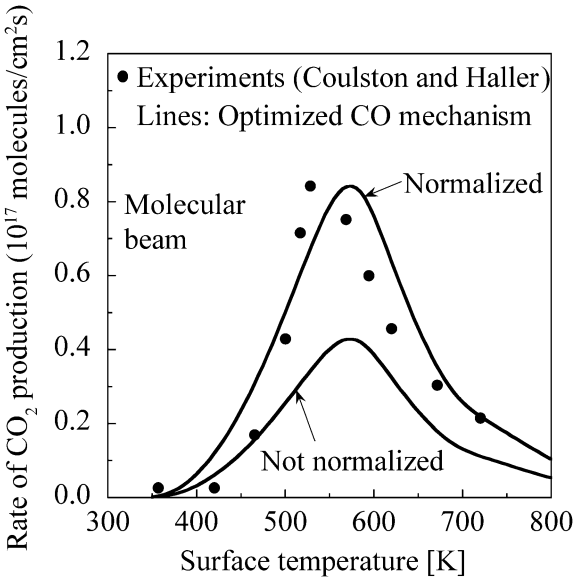

Fig. B.2. Assessment of the optimized CO mechanism against the molecular-beam experiments of [26]. The operating conditions include a CO flux of 1.1×10^{18} molecules/(cm^2 s) and a CO/O_2 ratio of 1/1. The predictions of the optimized mechanism, normalized against the experimental peak rate, are in good agreement with the data. Fair agreement (within a factor of two) is observed when the predictions are not normalized. No fitting of these data is done.

(MB1 and MB2 refer to experiments of [25] and [26], respectively) at different temperatures. The sensitivity coefficients are defined as $\mathrm{d}\ln R/\mathrm{d}\ln A$, where R is the model response and A is the pre-factor. The model responses are the ignition temperature for the ignition experiments and the CO_2 production rate for the molecular-beam experiments.

It is found that the adsorption–desorption of CO, the O_2 adsorption, and the surface reaction between CO^* and O^* are the most important steps. Because of a similar sensitivity in the two molecular-beam experiments, the second data set (MB2) can be considered as a redundant experiment and used for mechanism validation only. The CO-TPD [27] experiments depend only on the CO desorption pre-factor, as expected (not shown), whereas the CO oxidation TPR experiments of [29] are sensitive to the LH-type reaction between CO^* and O^* only (not shown); therefore they are also redundant and are used for validation.

Fig. A.2a shows the SA of the screening H_2 mechanism for our ignition data, and Fig. A.2b shows the SA for the LIF experiments of [5] at low and high temperatures. The model responses are the ignition temperature for ignition experiments and the OH mole fraction for the LIF experiments. Fig. A.2a shows that the adsorption–desorption of H_2 and O_2 and the surface reaction between H^* and O^* are the most important steps. For the LIF data, the model response is sensitive to the adsorption–desorption of O_2, the adsorption of H_2, and the desorption of OH (as expected), and at low temperatures it is affected to some extent by the loss of OH to $H_2O + O$. Again, the H_2-TPD [30] experiments depend only on the corresponding desorption pre-factor (not shown), whereas the H_2 oxidation TPR [33] experiments are sensitive only to LH-type reaction steps (not shown); therefore they are also redundant and are used for validation.

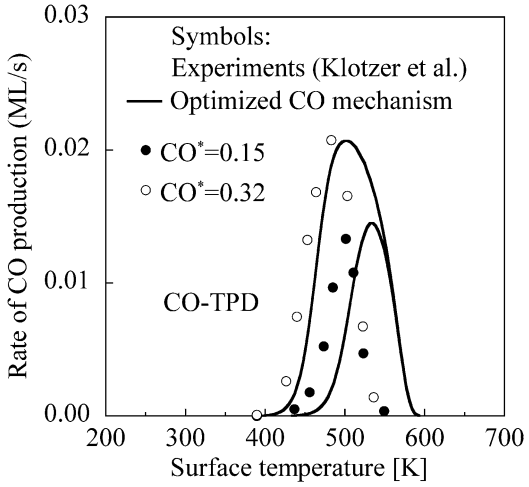

Fig. B.3. Assessment of the optimized CO mechanism against the CO-TPD data of [27] for two different initial CO^*-coverages indicated. The operating conditions include a pressure of 10^{-10} Torr and an assumed ramp rate of 15 K/s. The rate of CO production is normalized with the experimental peak rate. No fitting of these data is done.

Overall, the ignition, molecular-beam (MB1), and LIF experiments are selected as targeted experiments for optimization of the pre-factors of the mechanisms. These experiments represent a wide range of operating conditions, from atmospheric pressure to low pressures, and from low temperatures to high temperatures.

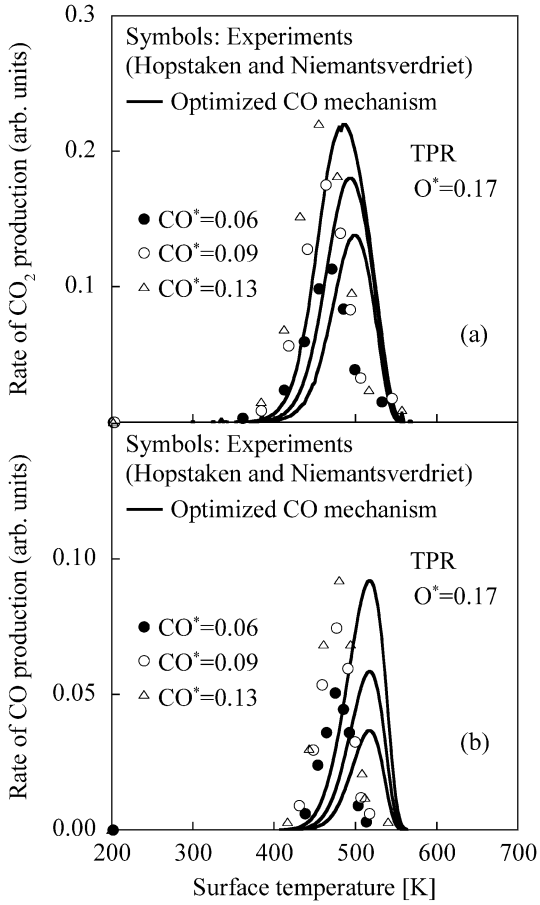

Fig. B.4. Assessment of the optimized CO mechanism against the TPR data of [29] for different initial coverages indicated. The operating conditions include a pressure of 7.5×10^{-11} Torr and a ramp rate of 5 K/s. The rates of CO_2 (a) and CO (b) production are normalized with the experimental peak rate (reported in arbitrary units). The simulated peak location and the shape of the TPR curve compare fairly well with the experiments. No fitting of these data is done.

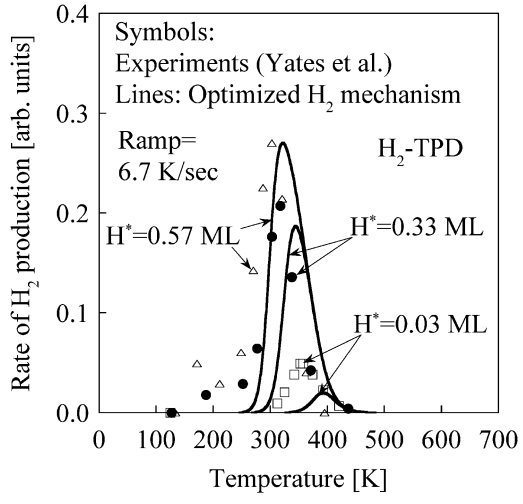

Fig. B.5. Assessment of the optimized H_2 mechanism against the H_2-TPD data of [30] for three different initial H^*-coverages indicated. The operating conditions include an initial temperature of 100 K and a ramp rate of 6.7 K/s [31]. The rate of H_2 production is normalized with the experimental peak rate. No fitting of these data is done.

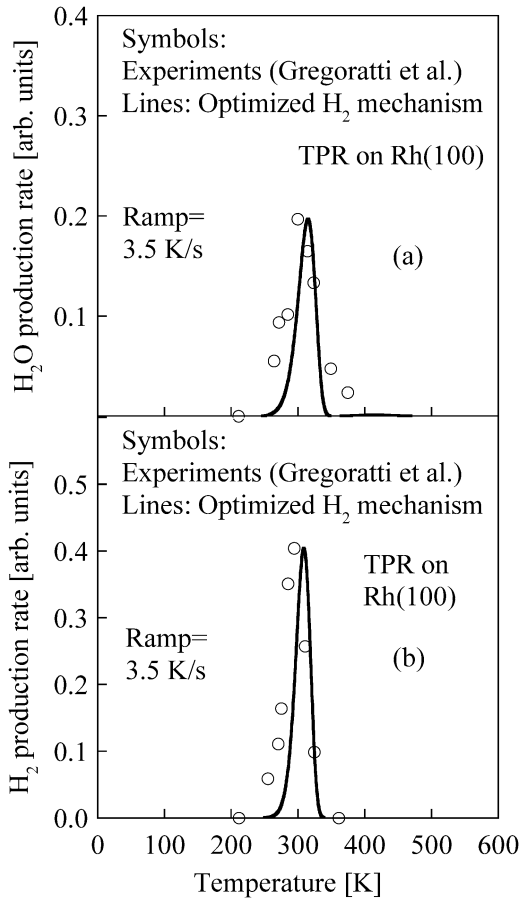

Fig. B.6. Assessment of the optimized H_2 mechanism against the TPR data of [33] on Rh(100). The operating conditions include an initial temperature of 200 K and a ramp rate of 3.5 K/s. The rates of H_2O and H_2 production are normalized with the experimental peak rates. No fitting of these data is done.

Appendix B. Assessment of reaction mechanisms against additional experimental data on Rh

Even though the optimized parameters capture the targeted experimental data, it is important to assess their performance against other redundant data sets, so that their validity under different operating conditions can be justified. Here we show the performance of the reaction mechanisms listed in Table 1 against some selected experiments discussed in the main paper.

Fig. B.1 shows the performance of the optimized CO mechanism against the molecular-beam experiments of [25] for different CO/O_2 compositions. Note that the targeted experimental data in Fig. 2 are for a different inlet composition of $CO/O_2 = 3/1$. The trends in the experimental data are fairly well captured in Fig. B.1. Fig. B.2 shows another validation against the molecular-beam experiments of [26]. The peak location is well predicted by the optimized microkinetic model. Finally, we present two more validations against CO-TPD [27] and TPR [29] data in Figs. B.3 and B.4, respectively. Good qualitative agreement between experimental data and mechanism predictions indicates that

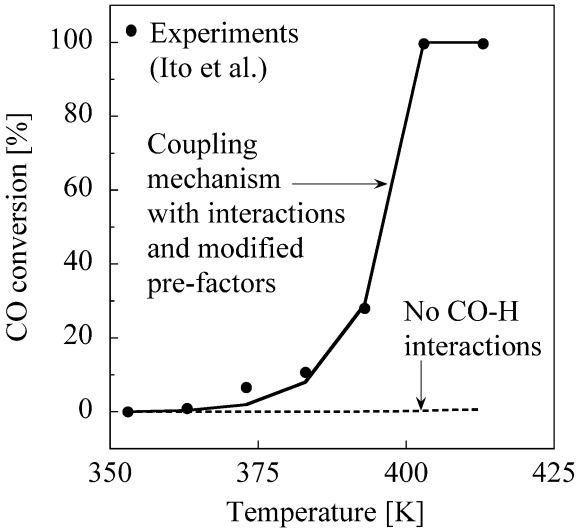

Fig. B.7. Predictions of the coupling mechanism with CO–H interactions and modified pre-factors against the CO PROX experimental data of [54]. The dashed line shows the lack of activity when the CO–H interactions are turned off. The operating conditions include a pressure of 1 atm, an assumed reactor length and diameter of 1 and 0.5 cm, respectively, an inlet flow rate of 100 cm^3/min at STP, and an inlet composition of 0.2% CO, 1% O_2, 3% H_2, and 95.8% He. A/V is adjusted to 40 cm^{-1}. No fitting of these data is done.

the heat of CO chemisorption, the coverage effects, and the activation energies of steps R_9–R_{10} are reasonably incorporated into the mechanism.

Similar validations for the optimized H_2 mechanism are shown in Figs. B.5 and B.6 against the H_2-TPD [30,31] and TPR [33] experiments, respectively. Good qualitative agreement is observed between the experimental data and the mechanism predictions.

Validation of the coupling mechanism with CO–H interactions and modified pre-factors is presented against the low-temperature PROX experiments of Ito et al. [54] in Fig. B.7. Figs. B.8a and B.8b show the predictions of the coupling mechanism against the CO PROX experimental data of [55] for the effect of inlet composition on CO conversion. Our coupling mechanism captures all considered data sets fairly well. The CO–H interactions play a significant role in providing high activity in these predictions (compare solid with dashed lines). For example, even if A/V is set very high, the experimental data at the lowest inlet CO mole fraction (0.002) are underpredicted by at least a factor of 2.

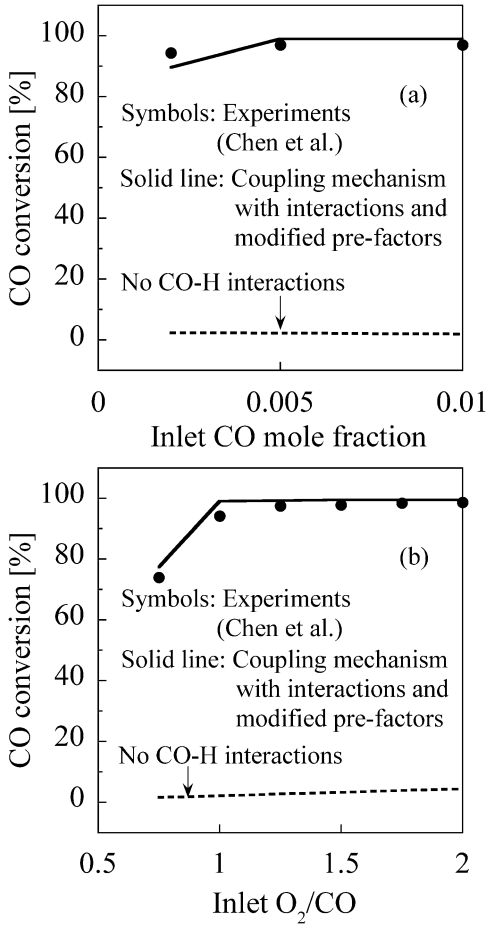

Fig. B.8. Predictions of the coupling mechanism with CO–H interactions and modified pre-factors against the CO PROX experimental data of [55]. The dashed lines show the minute activity when the CO–H interactions are turned off. The operating conditions include a pressure of 1 atm, a temperature of 500 K, a reactor volume of 0.88 cm^3, and a space velocity of 5×10^5 h^{-1} at STP. The dry feed stream contains 40% H_2, 20% CO_2, 0.2–1% CO, 0.2–1.5% O_2, with N_2 as balance. The mole ratio of H_2O to dry gas is 1:10. In panel (a), O_2/CO is equal to 1/1, whereas in panel (b), the inlet CO fraction is 0.5%. A/V is adjusted to 225 cm^{-1}. No fitting of these data is done.

References

[1] A.B. Mhadeshwar, D.G. Vlachos, J. Phys. Chem. B 108 (2004) 15246–15258.
[2] J.A. Dumesic, D.F. Rudd, L.M. Aparicio, J.E. Rekoske, A.A. Trevino, The Microkinetics of Heterogeneous Catalysis, American Chemical Society, Washington, DC, 1993.
[3] D.A. Hickman, L.D. Schmidt, AIChE J. 39 (7) (1993) 1164–1177.
[4] W.R. Williams, C.M. Marks, L.D. Schmidt, J. Phys. Chem. 96 (1992) 5922–5931.
[5] M.P. Zum Mallen, W.R. Williams, L.D. Schmidt, J. Phys. Chem. 97 (1993) 625–632.
[6] O. Deutschmann, R. Schmidt, F. Behrendt, J. Warnatz, Proc. Comb. Inst. 26 (1996) 1747–1754.
[7] M.P. Zum Mallen, L.D. Schmidt, J. Catal. 161 (1996) 230–246.
[8] P.-A. Bui, D.G. Vlachos, P.R. Westmoreland, Surf. Sci. 385 (2–3) (1997) 1029–1034.
[9] G. Veser, J. Frauhammer, Chem. Eng. Sci. 55 (12) (2000) 2271–2286.
[10] P. Aghalayam, Y.K. Park, N.E. Fernandes, V. Papavassiliou, A.B. Mhadeshwar, D.G. Vlachos, J. Catal. 213 (2003) 23–38.
[11] P. Aghalayam, Y.K. Park, D.G. Vlachos, in: Joint Combustion Meeting of the US Sections of the Combustion Institute, March 14–17, The Combustion Institute, Washington, DC, 1999, pp. 745–748.
[12] P. Aghalayam, Y.K. Park, D.G. Vlachos, in: J.J. Spivey (Ed.), Partial oxidation of Light Alkanes in Short Contact Time Microreactors, Catalysis, vol. 15, The Royal Society of Chemistry, Cambridge, UK, 2000, pp. 98–137.
[13] P. Aghalayam, Y.K. Park, D.G. Vlachos, AIChE J. 46 (10) (2000) 2017–2029.
[14] Y.K. Park, P. Aghalayam, D.G. Vlachos, J. Phys. Chem. A 103 (40) (1999) 8101–8107.

[15] S. Kandoi, A.A. Gokhale, L.C. Grabow, J.A. Dumesic, M. Mavrikakis, Cat. Lett. 93 (1–2) (2004) 93–100.
[16] N. Schumacher, A. Boisen, S. Dahl, A.A. Gokhale, S. Kandoi, L.C. Grabow, J.A. Dumesic, M. Mavrikakis, I. Chorkendorff, J. Catal. 229 (2005) 265–275.
[17] A.B. Mhadeshwar, H. Wang, D.G. Vlachos, J. Phys. Chem. B 107 (2003) 12721–12733.
[18] A.B. Mhadeshwar, D.G. Vlachos, Combust. Flame (2005), in press.
[19] P. Aghalayam, Y.K. Park, D.G. Vlachos, Proc. Combust. Inst. 28 (2000) 1331–1339.
[20] A.B. Mhadeshwar, D.G. Vlachos, Catal. Today 105 (2005) 162–172.
[21] S.R. Deshmukh, A.B. Mhadeshwar, M. Lebedeva, D.G. Vlachos, Int. J. Multiscale Comp. Eng. 2 (2) (2004) 221–238.
[22] S. Raimondeau, D.G. Vlachos, Chem. Eng. J. 90 (2002) 3–23.
[23] D.G. Vlachos, Adv. Chem. Eng. (2005), accepted for press.
[24] R. Sant, E.E. Wolf, Chem. Eng. Sci. 45 (10) (1990) 3137–3147.
[25] C.S. Gopinath, F. Zaera, J. Catal. 200 (2001) 270–287.
[26] G.W. Coulston, G.L. Haller, J. Chem. Phys. 95 (9) (1991) 6932–6944.
[27] B. Klotzer, W. Unterberger, K. Hayek, Surf. Sci. 532–535 (2003) 142–147.
[28] T.W. Root, L.D. Schmidt, Surf. Sci. 134 (1983) 30–45.
[29] M.J.P. Hopstaken, J.W. Niemantsverdriet, J. Chem. Phys. 113 (13) (2000) 5457–5465.
[30] J.T. Yates, P.A. Thiel, W.H. Weinberg, Surf. Sci. 84 (2) (1979) 427–439.
[31] S.H. Payne, H.J. Kreuzer, W. Frie, L. Hammer, K. Heinz, Surf. Sci. 421 (1999) 279–295.
[32] K.D. Gibson, M. Viste, S.J. Sibener, J. Chem. Phys. 112 (21) (2000) 9582–9589.
[33] L. Gregoratti, A. Baraldi, V.R. Dhanak, G. Comelli, M. Kiskinova, R. Rosei, Surf. Sci. 340 (1995) 205–214.
[34] D.H. Wei, D.C. Skelton, S.D. Kevan, Surf. Sci. 381 (1997) 49–64.
[35] J.T. Yates, P.A. Thiel, W.H. Weinberg, Surf. Sci. 82 (1) (1979) 45–68.
[36] A. Michaelides, P. Hu, J. Am. Chem. Soc. 123 (2001) 4235–4242.
[37] E. Shustorovich, H. Sellers, Surf. Sci. Report 31 (1998) 1–119.
[38] E. Shustorovich, Adv. Catal. 37 (1990) 101–164.
[39] A. Michaelides, Z.-P. Liu, C.J. Zhang, A. Alavi, D.A. King, P. Hu, J. Am. Chem. Soc. 125 (2003) 3704–3705.
[40] Z.-P. Liu, P. Hu, J. Chem. Phys. 115 (11) (2001) 4977–4980.
[41] J.K. Norskov, T. Bligaard, A. Logadottir, S. Bahn, E.W. Hansen, M. Bollinger, H. Bengaard, B. Hammer, Z. Sljivancanin, M. Mavrikakis, Y. Xu, S. Dahl, C.J.H. Jacobsen, J. Catal. 209 (2002) 275–278.
[42] S. Dahl, A. Logadottir, C.J.H. Jacobsen, J.K. Norskov, Appl. Catal. A: Gen. 222 (2001) 19–29.
[43] A. Logadottir, T.H. Rod, J.K. Norskov, B. Hammer, S. Dahl, C.J.H. Jacobsen, J. Catal. 197 (2001) 229–231.
[44] R.A. van Santen, J.W. Niemantsverdriet, Chemical Kinetics and Catalysis, Plenum Press, New York, 1995.
[45] V.P. Zhdanov, Surf. Sci. Report 12 (1991) 183–242.
[46] R. Schennach, G. Krenn, B. Klotzer, K.D. Rendulic, Surf. Sci. 540 (2003) 237–245.
[47] M. Beutl, J. Lesnik, K.D. Rendulic, Surf. Sci. 429 (1999) 71–83.
[48] T. Hrncir, V. Matolin, V. Nehasil, Surf. Sci. 482–485 (2001) 260–265.
[49] Visual-Numerics, IMSL FORTRAN subroutines for mathematical applications (1997).
[50] P. Panagiotopoulou, D.I. Kondarides, J. Catal. 225 (2004) 327–336.
[51] C. Wheeler, A. Jhalani, E.J. Klein, S. Tummala, L.D. Schmidt, J. Catal. 223 (2004) 191–199.
[52] T. Utaka, T. Okanishi, T. Takeguchi, R. Kikuchi, K. Eguchi, Appl. Catal. A: Gen. 245 (2003) 343–351.
[53] Y.-F. Han, M.J. Kahlich, M. Kinne, R.J. Behm, Appl. Catal. B: Env. 50 (2004) 209–218.
[54] S. Ito, T. Fujimori, K. Nagashima, K. Yuzaki, K. Kunimori, Catal. Today 57 (2000) 247–254.
[55] G. Chen, Q. Yuan, H. Li, S. Li, Chem. Eng. J. 101 (2004) 101–106.
[56] M. Mavrikakis (2004), personal communications.
[57] B. Hammer, O.H. Nielsen, J.J. Mortensen, L. Bengtsson, L.B. Hansen, A.C.E. Madsen, Y. Morikawa, T. Bligaard, A. Christensen, DACAPO version 2.7 (CAMP, Technical University, Denmark).
[58] A.B. Mhadeshwar, J.R. Kitchin, M.A. Barteau, D.G. Vlachos, Catal. Lett. 96 (1–2) (2004) 13–22.
[59] G.B. Fisher, S.J. Schmieg, J. Vacuum Sci. Technol. A 1 (2) (1983) 1064–1069.
[60] V.I. Savchenko, G.K. Boreskov, A.V. Kalinkin, A.N. Salanov, Kinet. Catal. 24 (5) (1983) 983–990.
[61] S. Wilke, V. Natoli, M.H. Cohen, J. Chem. Phys. 112 (22) (2000) 9986–9995.
[62] E.W. Hansen, M. Neurock, Surf. Sci. 441 (1999) 410–424.
[63] D. Loffreda, D. Simon, P. Sautet, J. Chem. Phys. 108 (15) (1998) 6447–6457.
[64] M. Smedh, A. Beutler, M. Borg, R. Nyholm, J.N. Anderson, Surf. Sci. 491 (2001) 115–123.
[65] R. He, H. Kusaka, M. Mavrikakis, J.A. Dumesic, J. Catal. 217 (2003) 209–221.
[66] P.A. Thiel, E.D. Williams, J.T. Yates, W.H. Weinberg, Surf. Sci. 84 (1) (1979) 54–64.
[67] C.J. Zhang, P. Hu, M.-H. Lee, Surf. Sci. 432 (1999) 305–315.
[68] M. Mavrikakis, M. Baumer, H.-J. Freund, J.K. Norskov, Catal. Lett. 81 (3–4) (2002) 153–156.
[69] H.A.C.M. Hendrickx, A.P.J.M. Jongenelis, B.E. Nieuwenhuys, Surf. Sci. 154 (2–3) (1985) 503–523.
[70] L.S. Brown, S.J. Sibener, J. Chem. Phys. 90 (5) (1989) 2807–2815.
[71] M.J. Hei, H.B. Chen, J. Yi, Y.J. Lin, Y.Z. Lin, G. Wei, D.W. Liao, Surf. Sci. 417 (1998) 82–96.
[72] S. Wilke, D. Hennig, R. Lober, Phys. Rev. B 50 (4) (1994) 2548–2564.
[73] M. Mavrikakis, J. Rempel, J. Greeley, L.B. Hansen, J.K. Norskov, J. Chem. Phys. 117 (14) (2002) 6737–6744.
[74] A. Eichler, J. Hafner, G. Kresse, J. Phys. Condens. Mater. 8 (1996) 7659–7675.
[75] J.J. Zinck, W.H. Weinberg, J. Vacuum Sci. Technol. 17 (1) (1980) 188–189.
[76] P.J. Feibelman, Phys. Rev. Lett. 90 (18) (2003) 186103–186103.